PCCP

ROYAL SOCIETY OF CHEMISTRY

PAPER

View Article Online
View Journal

Cite this: DOI: 10.1039/d6cp00605a

Intersystem crossing in 5-azacytosine: time-resolved photoelectron and quantum-chemical insights into the effect of aza substitution on cytosine

Bijay Duwal, [a] Antonio Carlos Borin *[b] and Susanne Ullrich *[a]

Received 18th February 2026,
Accepted 22nd May 2026

DOI: 10.1039/d6cp00605a

rsc.li/pccp

Single-atom substitutions in nucleobases can cause drastic changes in their photophysical response to ultraviolet radiation, in particular their propensity for intersystem crossing. Azabases are formed by replacing an endocyclic carbon atom with a nitrogen atom. 5-Azacytosine (5AC), an aza-derivative of cytosine with substitution at the C5 position of the ring, exists in both keto and enol tautomeric forms in the gas phase. However, most prior investigations have focused exclusively on the keto tautomer. In the present study, time-resolved photoelectron spectroscopy (TRPES) and extended multistate complete active space second-order perturbation theory, with double ξ-basis sets (XMS-CASPT2/cc-pVDZ) are employed to investigate the photophysics of both keto and enol forms of 5AC. The study finds that both tautomers preferentially undergo internal conversion (IC) to the ground state, with a measurable contribution from an intersystem crossing (ISC) pathway only in the keto form.

1. Introduction

Nucleobases are the chromophores of RNA and DNA, and their response to ultraviolet (UV) irradiation is characterized by ultrafast internal conversion (IC) to the ground state, which provides inherent photostability by dissipating electronic energy of reactive excited states as harmless heat.[1–5] Intersystem crossing (ISC) becomes relevant only on sufficiently long timescales. Slight structural modifications of nucleobases can significantly alter the topography of their potential energy surfaces and, consequently, change their electronic excited-state dynamics. Given the importance of nucleobases as the building blocks of the genetic code, there has been widespread interest in the photophysics of both canonical and structurally modified nucleobases.[6–9] Studying nucleobases with single-atom substitutions can help identify specific structural and electronic factors that affect the intrinsic photoprotective pathways of canonical nucleobases.

Substitution of an endocyclic carbon atom in a nucleobase with a nitrogen atom forms an azabase. Azabases can be broadly categorized into two groups: type A (*e.g.*, 6-azauracil and 8-azaadenine), characterized by significant triplet yield, and Type B (*e.g.*, 5-azacytosine and 8-azaguanine), characterized by negligible triplet yield.[10] In 6-azauracil, where the C_6 atom (double-bonded to C_5) of uracil is replaced by N_6, the photophysics are characterized by a near-unity triplet yield, unlike in uracil.[11–13] IC in uracil is promoted by conical intersections that involve stretching and/or twisting of the C_5═C_6 bond.[14,15] In fact, along the direct $S_2(^1\pi\pi^*)$ to S_0 pathway a strongly twisted hot GS intermediate has been identified.[16] However, aza-substitution at the C_6 position hinders twisting deformations of the C_5═N_6 bond, which would otherwise enable a similar direct decay pathway in 6-azauracil.[12] Instead ISC from the lowest $S_1(^1n\pi^*)$ state, or possibly directly from $S_2(^1\pi\pi^*)$ becomes efficient.[12,13] 6-azathymine, a derivative of 6-azauracil and an aza-analogue of thymine, features additional methylation at the C_5 atom. This molecule also exhibits two parallel decay pathways: IC from the bright $S_2(^1\pi\pi^*)$ state to the dark $S_1(^1n\pi^*)$ state followed by ISC to the triplet $T_1(^3\pi\pi^*)$ state, and direct ISC from the bright $S_2(^1\pi\pi^*)$ state to the triplet $T_2(^3n\pi^*)$ state followed by IC to the lower triplet $T_1(^3\pi\pi^*)$ state.[17] The triplet yield is 46%, approximately 30 times higher than that of thymine. 8-Azaadenine shows singlet-to-triplet decay very similar to that of 6-azauracil and 6-azathymine.[18] In contrast, 8-azaguanine exhibits efficient direct IC from the bright $S_1(^1\pi\pi^*)$ state to the ground state (GS), with negligible triplet-state population.[19] These differences in ISC behavior among the azabases have been attributed to characteristics of the lowest singlet $S_1(^1n\pi^*)$ state, which is often referred to as the "doorway" into the triplet manifold. Given the relevance of orbital localizations of the state in facilitating ISC in cytosine and its derivatives, a subscript O and N are used to indicate whether

[a] Department of Physics and Astronomy, University of Georgia, Athens, Georgia 30602, USA. E-mail: ullrich@uga.edu
[b] Department of Fundamental Chemistry, Institute of Chemistry, University of São Paulo, Av. Prof. Lineu Prestes, 748, São Paulo, 05508-000, São Paulo, Brazil. E-mail: ancborin@iq.usp.br

the non-bonding orbitals involved in the n → π* transition are localized on the oxygen (n_O) or nitrogen (n_N) atoms, respectively.

Unlike uracil and thymine, cytosine exists in multiple tautomeric forms under isolated gas-phase conditions.[20–22] The major tautomers of cytosine are the keto and enol forms, as shown in Fig. 1, panels a and b. To discern the excited state dynamics of different tautomers in time-resolved experiments, cytosine has been photoexcited in tautomer-specific or tautomer-dominant regions of its absorption spectrum.[23,24] For the keto form, IC from the bright $S_2(^1\pi\pi^*)$ state to the dark $S_1(^1n_O\pi^*)$ state and ISC to the triplet $T_1(^3\pi\pi^*)$ state occur in parallel with direct IC to the GS. The spin–orbit coupling (SOC) between the $S_1(^1n_O\pi^*)$ state and the triplet $T_1(^3\pi\pi^*)$ state is 30 cm^{-1}. In contrast, in the enol form, deactivation proceeds through IC from the bright $S_2(^1\pi\pi^*)$ state to the dark $S_1(^1n_N\pi^*)$ state, followed by IC from the latter to the GS—*i.e.*, limited to singlet states only. The SOC between the $S_1(^1n_N\pi^*)$ state and the triplet $T_2(^3n\pi^*)$ state is only 10 cm^{-1}.[25,26] The excited-state lifetime of the lowest singlet state S_1 in keto cytosine is strongly influenced by substitution around the C_5 atom.[27] The lifetime increases from approximately 1–3 ps in cytosine to 7.2 ps in 5-methylcytosine and 88 ps in 5-fluorocytosine, indicating that exocyclic substitution at C_5 slows down the efficient and ultrafast repopulation of the GS. This is not surprising, because the most favorable decay pathway to the GS, involving the $S_1(^1\pi\pi^*)$/GS conical intersection (CI) in keto cytosine, is characterized by twisting of the $C_5{=}C_6$ bond.[28] Nitrogen substitution at the C_5 position of the pyrimidine ring in cytosine forms 5-azacytosine (5AC), and this substitution is similarly expected to perturb the deactivation mechanism. The shorter $N_5{=}C_6$ bond length in keto 5AC compared to the $C_5{=}C_6$ bond in keto cytosine[29] indicates a strengthening of the double bond. Hence, a greater resistance to twisting of this double bond and a slowing down of the IC dynamics can be expected. Additionally, a reduced SOC in keto 5AC (13 cm^{-1}) compared to keto cytosine[30] suggests a lower tendency for ISC. Taking these considerations into account, one can anticipate overall longer excited-state lifetimes. To date, studies on the fundamental photophysical mechanisms of isolated 5AC are rare. Theoretical insights into the excited-state dynamics of 5AC have been limited to the N_1–H form of the keto tautomer only, while solution-phase experiments have largely neglected tautomeric aspects. However, 5AC predominantly exists as a mixture of keto and enol tautomers in the gas phase, as shown in Fig. 1, panels c and d. Boltzmann population ratios at standard ambient temperature can be determined based on the relative stabilities of the tautomers. Depending on the level of theory, energy differences of 0.5–1.2 kcal mol^{-1} have been reported for isolated 5AC.[22] Assuming an MP2/6-31G(d,p) energy difference of 0.5 kcal mol^{-1}, the Boltzmann population ratio of isolated keto (N_1–H) and enol tautomers at ambient temperature is approximately 30% and 70%, respectively. For hydrated 5AC complexes, assuming an MP2/6-31G(d,p) energy difference of 0.2 kcal mol^{-1} between the two keto forms (N_1–H and N_3–H), nearly equal populations (42% and 58%, respectively) are expected. The enol tautomer is significantly higher in energy in the hydrated complex and is therefore not relevant.

In the present study, time-resolved photoelectron spectroscopy (TRPES) and XMS-CASPT2/cc-pVDZ calculations are employed to investigate the gas-phase excited-state dynamics of 5AC. The aim is to explore the electronic excited-state behavior of the predominant keto and enol forms, which is achieved by exciting 5AC at various pump wavelengths across the absorption spectrum where tautomer contributions vary. A thorough steady-state analysis of the gas-phase absorption spectrum provides the basis for interpretation of the TRPES results. Most notably, this gas-phase TRPES study provides insight into the photodynamics of 5AC from a different tautomer perspective—that is, the N_1–H keto and enol tautomers—which are not accessible in time-resolved experiments performed in solution.

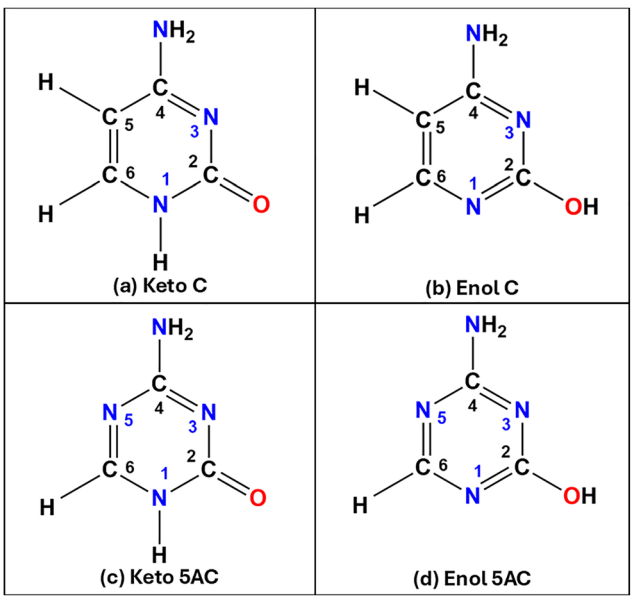

Fig. 1 Structure of the dominant cytosine (C) and 5-azacytosine (5AC) tautomers under gas phase conditions. Both cytosine and 5-azacytosine predominantly exist in keto (with a carbonyl group) and enol (with a hydroxyl group) tautomeric forms. (a) Keto cytosine; (b) Enol cytosine; (c) Keto 5-azacytosine; (d) Enol 5-azacytosine.

2. Method

2.1. Experimental details

The gas-phase absorption spectrum of 5AC is measured using a custom-built UV-vis spectrometer. The setup features a deuterium lamp (L2D2, Hamamatsu Co.) as the UV-visible light source, which is collimated by a plano-convex lens (focal length: 40 mm) and directed through a stainless-steel cell with a window-to-window path length of approximately 350 mm. The transmitted light is then focused by another plano-convex lens (focal length: 30 mm) and coupled into a fiber-optic spectrometer (HR4000, Ocean Optics, Inc.). Spectral data are acquired using the OceanView software (Ocean Optics, Inc.) with typical integration times of 100 ms. The gas-phase absorption spectrum is collected as follows: the sample is placed inside the cell, which is then

vacuum-sealed and pumped to rough vacuum. A reference spectrum of the lamp and a background spectrum are first recorded through the cell. Next, the cell is heated to approximately 300 °C using a rope heater to evaporate the sample, and the sample spectrum is recorded using the same integration time. The UV-vis absorption spectrum of the sample is then obtained as the logarithm of the ratio of the reference spectrum to the sample spectrum. Additionally, gas-phase Fourier-transform infrared (FTIR) spectra are obtained by installing a custom-built gas-cell assembly in the sample compartment of a FTIR spectrometer (Nicolet iS20, Thermo Fisher Scientific Inc.) along the infrared beam path. The sample is inserted into the cell, which has CaF_2 windows on both ends, then pumped to rough vacuum and heated with a rope heater. The Fourier transforms of the IR interferogram signals of both the sample and the background are recorded, and the logarithm of their ratio yields the sample spectrum.

The TRPES experiment has been described in detail elsewhere;[31–33] therefore, only a brief overview is provided here. The setup includes a Ti:Sa oscillator (Mira 900, Coherent Inc.) that seeds a regenerative amplifier (Legend Elite, Coherent Inc.), which in turn pumps two optical parametric amplifiers (OPerA, Coherent Inc.; TOPAS-C, Light Conversion Inc.) capable of producing tunable UV pulses. The output from the OPerA, serving as photoexciting pump pulses for the 5-azacytosine (J&K Scientific, 98%) sample, is set to wavelengths of 267 nm, 260 nm, 250 nm, and 243 nm, with a pulse energy of 2.0 μJ per pulse. Additionally, photoionizing probe pulses are provided by the TOPAS-C, tuned to 310 nm with a pulse energy of approximately 6.0 μJ per pulse. The pump and probe beams are focused independently using lenses with focal lengths of 50 cm and 40 cm, respectively, and intersect in the ionization region of a magnetic bottle photoelectron spectrometer. The sample powder, held in a quartz sample holder within the molecular beam vacuum chamber, is evaporated at 220 °C and is co-expanded with helium through a pinhole nozzle. The continuous molecular beam enters the ionization region of the spectrometer through a skimmer. Time-of-flight measurements of photoelectrons are conducted at various pump–probe delays, starting with a step size of 25 fs within a range from −1 to 4 ps, followed by gradually increasing step sizes up to a maximum delay of 3 ns. Shutters are installed in the pump and probe beams, and the pump-only and probe-only spectra are recorded throughout the entire scan for background subtraction from the pump–probe spectra. Each scan consists of four back-and-forth sweeps to minimize the effect of slow signal drifts and is reproduced at least twice. Timing and energy calibrations are performed using TRPES measurements of 1,3-butadiene. Calibration constants are derived from known vibrational features of the cation[34] to convert time-of-flight data into electron kinetic energy. The instrument response function, modeled as a Gaussian, has a full width at half maximum of approximately 200 fs for all pump wavelengths. Global analysis of the TRPES spectra is conducted using Glotaran,[35] employing a sequential decay model with three exponential components for the global fit. All other data analyses are performed using Origin.[36]

2.2. Theoretical details

Calculations are performed using Extended Multistate Complete Active Space Second-Order Perturbation Theory (XMS-CASPT2)[37,38] and the cc-pVDZ (correlation consistent polarized valence double-ξ) one-electron basis set.[39] XMS-CASPT2 calculations employ the standard zeroth-order Hamiltonian,[40] with frozen core orbitals and no IPEA shift correction,[41] as recommended in the literature.[42] Intruder states are treated using the imaginary level-shift (0.3 au) technique.[42] All computations are carried out using the OpenMolcas[43] software, with no symmetry constraints imposed. The Cholesky decomposition technique with unbiased auxiliary basis sets is used to speed up accurate two-electron integral evaluation.[44–46] Geometry optimizations for the ground and excited states are performed at the XMS-CASPT2/cc-pVDZ level, using a zeroth-order State Average Complete Active Space Self-Consistent-Field (SA-CASSCF)[47] wavefunction. For the keto tautomer, the zeroth-order wavefunction is averaged over the lowest six singlet and six triplet electronic states, with an active space (Fig. S1 in SI) including eight π and π* orbitals, plus three lone-pair orbitals (XMS(6S;6T)-CASPT2(16,11)/cc-pVDZ). For the enol tautomer, the lowest seven singlet (7S) and seven triplet (7T) electronic states are included in the averaging procedure, with an active space (Fig. S2 in SI) encompassing all π and π* orbitals and electrons, plus the non-bonding nitrogen (n_N) lone-pair orbitals (XMS(7S;7T)-CASPT2(14,10)/cc-pVDZ). The selected active spaces directly reflect the underlying chemical differences between the two tautomers. In the keto form, a lone-pair orbital localized on the carbonyl oxygen (n_O) is present and is essential in the active space to correctly describe the $n_O \rightarrow \pi^*$ excitation. This orbital is absent in the enol form. It is worth noting that OpenMolcas does not average over density matrices of different spin and spatial symmetries, so singlet and triplet states are computed separately. Vertical excitation energies are computed at the same level of theory. Oscillator strengths are obtained using transition dipole moments (length representation) *via* the CAS State Interaction (CASSI) method,[48] with electronic state energies computed at the XMS-CASPT2/cc-pVDZ level and perturbatively modified electronic wavefunctions.

Conical intersection and minimum-energy singlet–triplet crossing structures are optimized at the XMS-CASPT2/cc-pVDZ-DK level. For the conical intersections, analytic gradients and derivative coupling vectors are computed using the computational techniques implemented by Nishimoto, Battaglia, and Lindh.[49] Spin–orbit coupling (SOC) matrix elements are calculated using the Atomic Mean Field Integrals (AMFI)[50–52] approximation as implemented in the RASSI (Restricted Active Space State Interaction) module of OpenMolcas. Due to the computational cost of minimum-energy path calculations, characteristic points (minima and minimum-energy crossing points) on the potential energy hypersurfaces are connected using linear interpolation in geodesic coordinates.[53] Note that geodesic scans represent an upper bound to the actual path and may therefore overestimate energetic barriers. For critical points along the deactivation pathway, vertical ionization energies and Dyson intensities are computed following recent literature procedures[54] and implemented in the RASSI module.

For simulations of the absorption spectrum, the initial conditions are obtained by optimizing the ground-state equilibrium geometry at the XMS(7)-CASSCF(14,10)/cc-pVDZ level, followed by harmonic frequency calculation. A quantum harmonic oscillator Wigner distribution[55,56] of the lowest vibrational state is generated, from which 100 uncorrelated geometries and velocities are sampled. For each sampled geometry, vertical excitation energies are calculated at the same level of theory. The absorption spectrum is then constructed as a superposition of Gaussian functions centered at the computed vertical excitation energies, with heights proportional to oscillator strengths. Additionally, IR spectra of both the keto and enol tautomers of 5AC are computed at the MP2/cc-pVTZ level of theory.

3. Results and discussion

3.1. UV-vis absorption spectrum and relevant transitions

UV-vis absorption spectra of 5AC have previously been reported only in the solution phase. As discussed above, solvent interactions not only shift the absorption bands but also influence the tautomer presence and their relative populations. In aqueous solution, the Boltzmann distribution estimates nearly equal populations of two keto tautomers (N_1–H and N_3–H forms), while the enol tautomer is largely absent. In contrast, under gas-phase conditions, the N_1–H keto and enol tautomers dominate, whereas all other forms (including the N_3–H keto tautomer) are negligible. This highlights the importance of conducting steady-state absorption measurements under isolated conditions as a basis for interpreting the wavelength-dependent TRPES results.

The simulated and experimental gas-phase absorption spectra in Fig. 2 serve to identify the underlying electronic transitions and tautomer contributions at the selected pump wavelengths. Fig. 2(a) presents the simulated gas-phase UV-vis spectra of the keto (blue) and enol (red) tautomers of 5AC, computed at the XMS(6S;6T)-CASPT2(16,11)/cc-pVDZ and XMS(7S;7T)-CASPT2(14,10)/cc-pVDZ levels of theory, respectively. The vertical excitation energies of the singlet states are indicated by vertical lines (blue for keto and red for enol), with line heights corresponding to oscillator strengths (see Table 1). Simulations of the contributions from individual electronic states to these absorption spectra are provided in Fig. S3 in the SI. As shown in these spectra, the lowest bright singlet state—$^1\pi\pi^*$ (which may be S_1 or S_2 in Fig. S3)—of both the keto and enol tautomers is predominantly excited at the employed excitation wavelengths. To obtain semi-quantitative insight into tautomer contributions at different excitation wavelengths, the simulated tautomer spectra are fit to the experimental gas-phase absorption spectrum of 5AC using composite linear regression. Given the visible discrepancy between the simulated and experimental UV-vis spectra toward high excitation energies, the regression analysis is performed over the experimentally relevant energy range from 4 eV to 5.6 eV associated with the first absorption band. Fig. 2(b) shows the experimental gas-phase UV-vis absorption spectrum of 5AC in vacuum (black curve), overlaid with the simulated spectra of the keto (blue) and enol (red) tautomers weighted by the

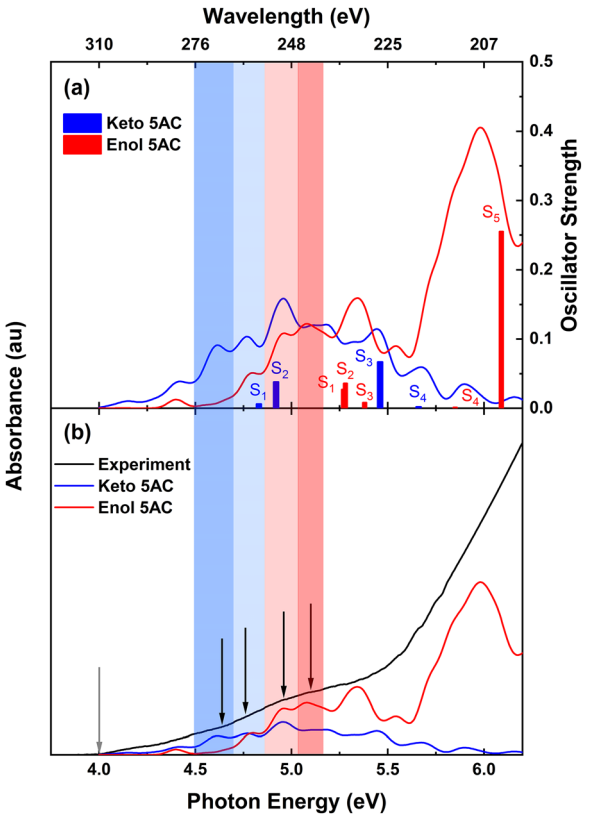

Fig. 2 UV-vis absorption spectra of 5-azacytosine. (a) The blue and red curves show the simulated UV-vis absorption spectra of keto and enol 5AC, respectively. Blue and red vertical lines indicate the computed vertical excitation energies from the ground state minimum to the electronic states, with line heights corresponding to oscillator strengths (Table 1). The blue and red shaded regions denote the spectral contributions of keto and enol 5AC according to the ratios in Table 3. (b) The black curve shows the experimental gas-phase UV-vis absorption spectrum of 5AC. The blue and red curves represent the simulated spectra of keto and enol 5AC, respectively, weighted using coefficients obtained from composite linear regression of the simulated tautomer spectra to the experimental spectrum. Black arrows indicate the photon energies of the pump pulses, while the grey arrow marks the photon energy of the probe.

regression coefficients, 0.018 and 0.037 with standard deviations of 0.003 and 0.002, respectively. The proportion of these coefficients approximates the tautomer population ratios of the tautomers in the molecular beam. The resulting population ratios of keto and enol 5AC are 33% and 67%, respectively. These values may be compared to Boltzmann population ratios of 5% : 95% at room temperature and 18% : 82% at 300 °C, based on the XMS-CASPT2 energy difference of 1.7 kcal mol^{-1} between the two tautomers. An energy difference of 0.5 kcal mol^{-1} from MP2 calculation yields keto : enol population ratios of approximately 39% : 61% at 300 °C, which are in close agreement with the regression analysis.[22] Overall, the sum of the weighted simulated spectra reproduces the general shape of the experimental absorption spectrum for the region of interest.

To interpret the TRPES data, knowledge of the tautomer contributions at specific pump wavelengths is essential. The pump wavelengths (267 nm, 260 nm, 250 nm, and 243 nm) are

Table 1 Electronic character, vertical excitation energy, and oscillator strength of relevant singlet and triplet states of keto and enol 5AC, computed at the XMS(6S;6T)-CASPT2(16,11)/cc-pVDZ and XMS(7S;7T)-CASPT2(14,10)/cc-pVDZ levels of theory, respectively

Tautomers	Keto			Enol		
States	Electronic character	Vertical excitation energy (eV)	Oscillator strength	Electronic character	Vertical excitation energy (eV)	Oscillator strength
S_1	$^1n_N\pi^*$	4.83	0.006	$^1n_N\pi^*$	5.27	0.027
S_2	$^1\pi\pi^*$	4.92	0.038	$^1\pi\pi^*$	5.28	0.036
S_3	—	5.46	0.067	$^1n_N\pi^*$	5.38	0.008
S_4	—	5.66	0.002	$^1n_N\pi^*$	5.85	0.001
S_5	—	5.83	0.000	$^1\pi\pi^*$	6.09	0.255
S_6	—	—	—	$^1n_N\pi^*$	6.21	0.018
T_1	—	—	—	$^3\pi\pi^*$	4.82	—
T_2	—	—	—	$^3n_N\pi^*$	5.04	—
T_3	—	—	—	$^3\pi\pi^*$	5.21	—
T_4	—	—	—	$^3n_N\pi^*$	5.24	—
T_5	—	—	—	$^3n_N\pi^*$	5.58	—
T_6	—	—	—	$^3n_N\pi^*$	5.75	—
T_7	—	—	—	$^3n_N\pi^*$	5.96	—

selected to excite the first bright states of both tautomers, while the probe wavelength (310 nm) is chosen to avoid probe-pump signals. The weighted simulated UV-vis spectra (Fig. 2b) enable estimation of the photoexcited keto : enol tautomer ratio at each pump wavelength, as summarized in Table 3. Comparing the experimental and simulated spectra shows that the keto tautomer is selectively excited at 267 nm, which lies at the onset of the experimental absorption spectrum. The 260 nm pump coincides with the enol onset, and at higher photon energies (250 nm and 243 nm), both tautomers are expected to be excited simultaneously, with increasing contributions from the enol tautomer. The presence of both keto and enol tautomers in the gas phase is further supported by the FTIR spectrum in Fig. S6 in the SI. The keto : enol ratios listed in Table 3 for different pump wavelengths should be considered approximate, due to several sources of uncertainty. Experimental factors include different gaseous sample preparation methods—gas cell *versus* molecular beam—for the UV-vis and TRPES measurements, respectively. Even if the sample is heated to a similar temperature, additional collisional cooling during the molecular beam expansion may alter the keto : enol tautomer ratio. Estimation of Boltzmann population ratios is limited by the accuracy of *ab initio* methods in predicting relative tautomer stabilities, which differ among the XMS-CASPT2, MP2, and CCSD levels of theory considered here. Furthermore, the composite linear regression analysis of the gas-phase absorption spectrum depends on accurate simulation of tautomer-specific spectra, which becomes challenging for contributions from higher-lying excited states. The strong second absorption band in 5AC is significantly red shifted in the simulations, which may influence the optimization and conversion of the composite linear regression. To minimize this effect, the regression analysis is performed over the region primarily associated with the first absorption band up to an energy of 5.6 eV. For comparison, the regression analysis is also performed using two Gaussian functions representing the simulated keto and enol absorption bands to eliminate the effect of spectral features on the determination of tautomer ratios (see SI, Fig. S4). The extracted wavelength-dependent ratios are, on average, within ±10% of the values reported in Table 3. Despite these uncertainties, the agreement among the various approaches is sufficient to provide qualitative guidance for the analysis of the TRPES.

3.2. Geodesic interpolated pathways

Based on the computations for enol 5AC, the first two singlet states, S_2 ($^1\pi\pi^*$) and S_1($^1n_N\pi^*$), are bright in absorption with comparable oscillator strengths, and are close in energy. This suggests that either state can be initially photoexcited by the pump pulse. Due to their energetic proximity, a minimum energy conical intersection (MECI) exists between these states—S_2($^1\pi\pi^*$)/S_1($^1n_N\pi^*$)$_{MECI}$—which lies within the Franck–Condon (FC) region and enables ultrafast population transfer. If the pump pulse initially excites the S_2($^1\pi\pi^*$) state, it rapidly decays to the S_1($^1n_N\pi^*$) state. Thus, the most important photophysical processes proceed from the S_1($^1n_N\pi^*$) state regardless of which state is initially photoexcited. Fig. 3 shows the geodesic interpolated pathway from the FC region to the minimum of the S_1($^1n_N\pi^*$) potential energy surface, S_1($^1n_N\pi^*$)$_{min}$, which is characterized by an envelope-like geometry with puckering of the C_6 atom out of the molecular plane. Along this coordinate, the S_1($^1n_N\pi^*$) state

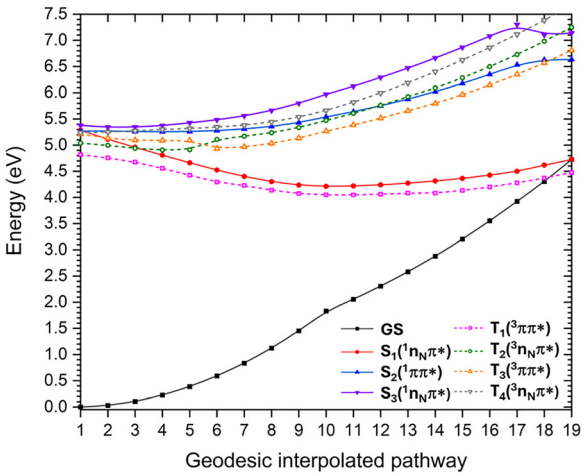

Fig. 3 Geodesic interpolated pathways for the enol tautomer of 5AC.

evolves barrierless from the $S_2(^1\pi\pi^*)/S_1(^1n_N\pi^*)_{MECI}$ region to the equilibrium structure, $S_1(^1n_N\pi^*)_{min}$, located adiabatically at about 4.05 eV above the ground state minimum (GS_{min}) and about 1.23 eV below the FC region. The geodesic interpolated pathway starting from $S_1(^1n_N\pi^*)_{min}$ region indicates an accessible CI with the GS, $S_1(^1n_N\pi^*)/GS_{MECI}$, located adiabatically about 4.72 eV above the GS_{min} (vertically 0.67 eV above the $S_1(^1n_N\pi^*)_{min}$, and 0.56 eV below the FC region). This CI, also characterized by C_6 puckering, facilitates ultrafast and radiationless population transfer to the GS. Alternative pathways involving intersystem crossing have been considered. As can been seen in Fig. 3, a $S_2(^1\pi\pi^*)/T_3(^3\pi\pi^*)_{MECI}$ singlet–triplet crossing is identified near the FC region (point 1). However, according to Kasha's rule, ISC in this region is unlikely. Instead, the barrierless evolution along the singlet states towards the $S_1(^1n_N\pi^*)_{min}$ will outcompete this ISC process. An extensive search for a $S_1(^1n_N\pi^*)/T_1(^3\pi\pi^*)$ crossing was conducted, but no crossing point could be identified. Farther along the interpolated pathway, another crossing with the $T_1(^3\pi\pi^*)$ state (point 18)—$T_1(^3\pi\pi^*)/GS_{MECI}$—is found at 4.37 eV adiabatically above the GS_{min}, in the vicinity of $S_1(^1n_N\pi^*)/GS_{MECI}$ CI region (point 19). The computed SOC ($\sim$15 cm^{-1}) in this region suggests that ISC to the $T_1(^3\pi\pi^*)$ state is possible. However, once the system reaches the $S_1(^1n_N\pi^*)/GS_{MECI}$ region, the electronic population relaxes to the GS_{min} on a timescale much faster than the ISC process, making population of the $T_1(^3\pi\pi^*)$ state an unlikely channel. In summary, the calculations predict that the excited-state dynamics of the enol tautomer are dominated by IC processes, with ISC contributing negligibly.

This behavior is distinctly different from the previously reported deactivation mechanism for keto 5AC in the gas phase.[30] Briefly, after photoexcitation to the bright $S_2(^1\pi\pi^*)$ state, the keto tautomer undergoes IC to $S_1(^1n_N\pi^*)$. From there, two CIs with distinct geometric characteristics provide access to the GS: (1) a boat-like conformation of the ring in which N_3 and C_6 are displaced from the molecular plane in the same direction (with a barrier of 0.07 eV), and (2) a half-chair conformation in which the N_5 and C_6 are displaced from the ring plane in opposite directions, along with an envelope-like geometry involving the displacement of C_6 out of the ring plane (with a barrier of 0.28 eV). In keto 5AC, although the energy barrier between the $S_1(^1n_N\pi^*)_{min}$ and the crossing point between $S_1(^1n_N\pi^*)$ and $T_1(^3\pi\pi^*)$ is less than 0.02 eV, ISC remains only a minor relaxation channel due to relatively small SOC of 13 cm^{-1}. The ISC yield is estimated at 10 $\pm$ 8%. The lower SOC in keto 5AC compared to keto cytosine (SOC of 40 cm^{-1}) is attributed to the localization of the nonbonding orbital of the $S_1(^1n\pi^*)$ state on the N_5 atom in keto 5AC ($^1n_N\pi^*$) rather than on the O atom, as is the case for keto cytosine ($^1n_O\pi^*$). Compared to enol 5AC, these calculations predict a more complex IC mechanism for the keto tautomer, including clear signatures of ISC.

3.3. TRPES

Fig. 4 illustrates the time-resolved photoelectron spectra of 5AC. The first and second columns depict the TRPES signals and energy-integrated time traces, respectively, with the latter extracted from global analysis based on a sequential decay model with three exponentials. While the theoretical deactivation model for the keto tautomer suggests a branching decay, the use of such a model is not practical and would lead to overparameterization of the fit. Due to the broadband nature of the femtosecond pulses, the TRPES bands are broad and featureless with overlapping contributions from excited state processes of both tautomers. In the absence of clear spectral fingerprints and/or very distinct timescales of the different deactivation channels and tautomers, these contributions cannot be disentangled with global lifetime analysis. A sequential model is therefore deemed the best choice to capture the consecutive nature of the deactivation process. Additional fit results and justification of the fitting model are available in the SI, Fig. S7–S9. TRPES is sensitive to the orbital character of electronically excited states *via* Koopman's like ionization correlations to different cationic states and can provide insight into population dynamics along the deactivation pathway. Two factors need to be taken into account when estimating the electron binding energy (eBE) range of photoelectron bands arising from ionization at different points along the relaxation pathway. First, changes in the ionization potential and ionization preferences occur along this pathway. Second, there is also a propensity for vibrational excitations of the neutral state to be preserved in the ionization process and transferred to the cationic state. The squares and circles on the TRPES signal plots delineate the estimated eBE ranges corresponding to ionization from the FC region and different excited state minima for the keto and enol tautomers, respectively. Specifically, the magenta symbols with black and white outlines are correlated with the $FC(^1\pi\pi^*)$ region and minimum of the $S_2(^1\pi\pi^*)$, respectively, the green symbols with the $S_1(^1n_N\pi^*)_{min}$, and the blue symbols with the $T_1(^3\pi\pi^*)_{min}$. The eBE estimates are derived from excited-state energies, vibrational energy gains during electronic relaxation, and ionization energies at the different geometries, computed at the XMS-CASPT2/cc-pVDZ level (see Table S2 in the SI for details about the calculations). These calculation-based values assume an initial vertical excitation from the GS_{min} to the FC region of the $S_2(^1\pi\pi^*)$. For analysis of the TRPES at different pump wavelengths, the eBE estimates are adjusted by the difference in pump photon energy relative to the vertical excited state energies (Table S3 in the SI). This accounts for varying amounts of vibrational excess energy as the pump wavelength is tuned, which manifests itself in a systematic shift of the entire TRPES signal and is clearly visible in Fig. 4. Table 3 summarizes the time constants corresponding to the population decay dynamics of the different excited states. The reported time constants and errors are derived from the analysis of multiple scans at a particular pump wavelength and thus indicate the reproducibility of the time constants.

3.4. Assignment of the photoelectron spectra of keto-only TRPES of 5AC

The pump wavelength of 267 nm lies at the onset of the experimental UV-vis absorption spectrum of 5AC. This wavelength corresponds to the narrow spectral region with significant keto absorption (Fig. 2). This is reflected in the estimated 0.84 : 0.16 keto-to-enol ratio of photoexcited 5AC based on composite linear regression analysis (Table 3). Hence, with a 267 nm

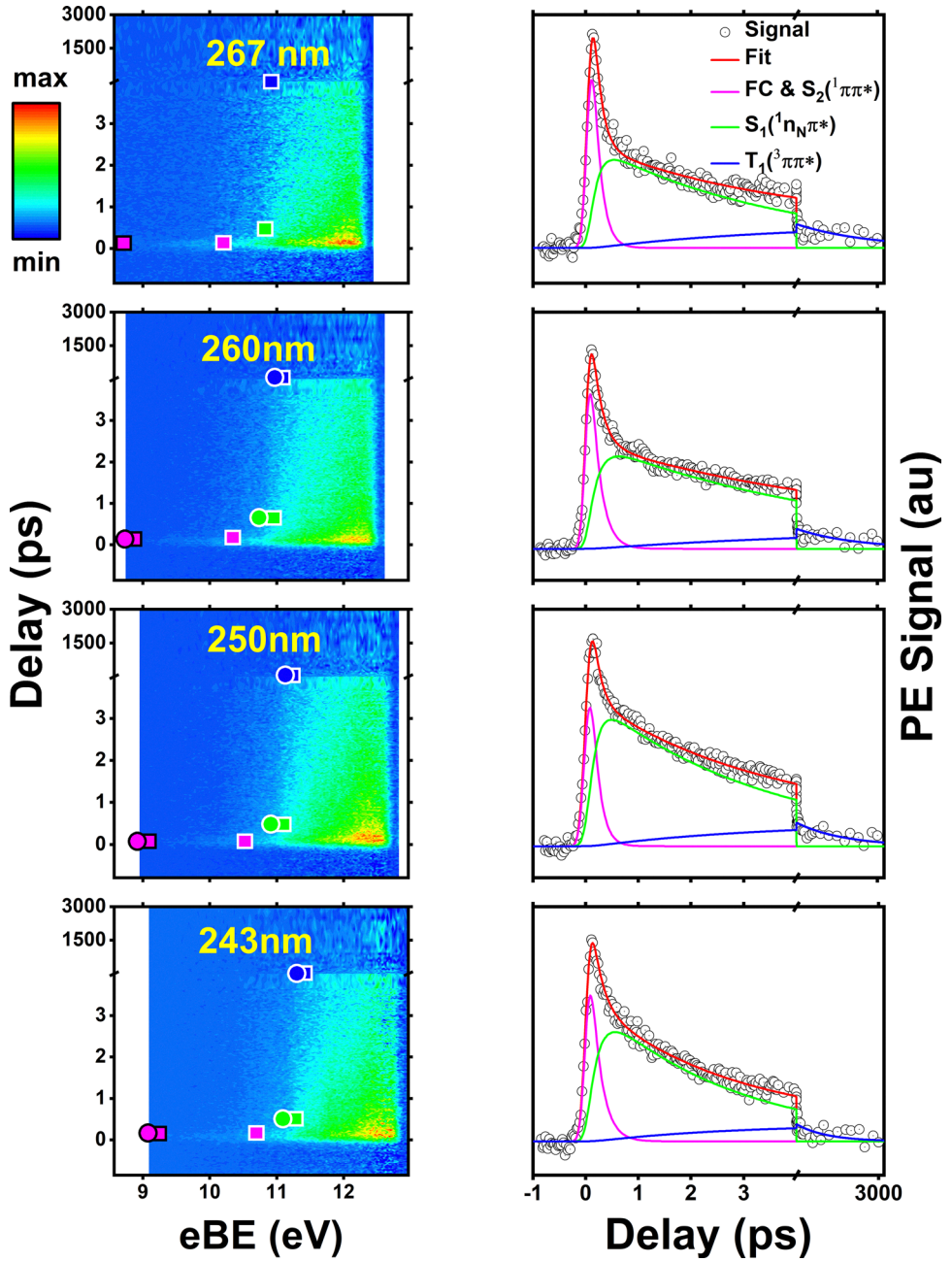

Fig. 4 TRPES of 5-azacytosine in the gas phase. The first column shows the time-resolved photoelectron spectra (electron binding energy *versus* pump–probe delay, with axis break at 4 ps), plotted as colormaps, with each row corresponding to a specific pump–probe wavelength combination. Colored squares/circles mark the electron binding energies where photoelectron bands for ionization from different excited states are expected (magenta—$S_2(^1\pi\pi^*)$, green—$S_1(^1n_N\pi^*)_{min}$, blue—$T_1(^3\pi\pi^*)_{min}$). Squares indicate estimates for the keto tautomer, whereas circles indicate those for the enol tautomer. A black *versus* white outline distinguishes the FC region and minimum of the $S_2(^1\pi\pi^*)$ state, respectively. The second column shows energy-integrated time traces (photoelectron signal *versus* delay) extracted from global lifetime analysis. In these time traces, the magenta, green, and blue components denote population decays from the FC region and $S_2(^1\pi\pi^*)_{min}$, from $S_1(^1n_N\pi^*)_{min}$, and from $T_1(^3\pi\pi^*)_{min}$, respectively.

(4.64 eV) pump, the bright $S_2(^1\pi\pi^*)$ state of keto 5AC is excited with approximately 0.17 eV of excess vibrational energy. The first time constant of 160 fs, obtained from the global analysis of the TRPES, measures the population decay of this state. This interpretation is confirmed by the observed photoelectron band, which originates at an eBE associated with ionization in the FC$(^1\pi\pi^*)$ region, but due to rapid relaxation, is only captured with weak intensity. It evolves into a more intense band toward higher eBE (Fig. 5, second column) and extends beyond the region associated with ionization from the $S_2(^1\pi\pi^*)_{min}$. High-level *ab initio* calculations of the excited state potentials have identified two relevant *CIs* that lead from the $S_2(^1\pi\pi^*)$ either to the lower $S_1(^1n_N\pi^*)$ or directly to the GS. The latter CI is located in the vicinity of the $S_2(^1\pi\pi^*)_{min}$. However, dynamics simulations have

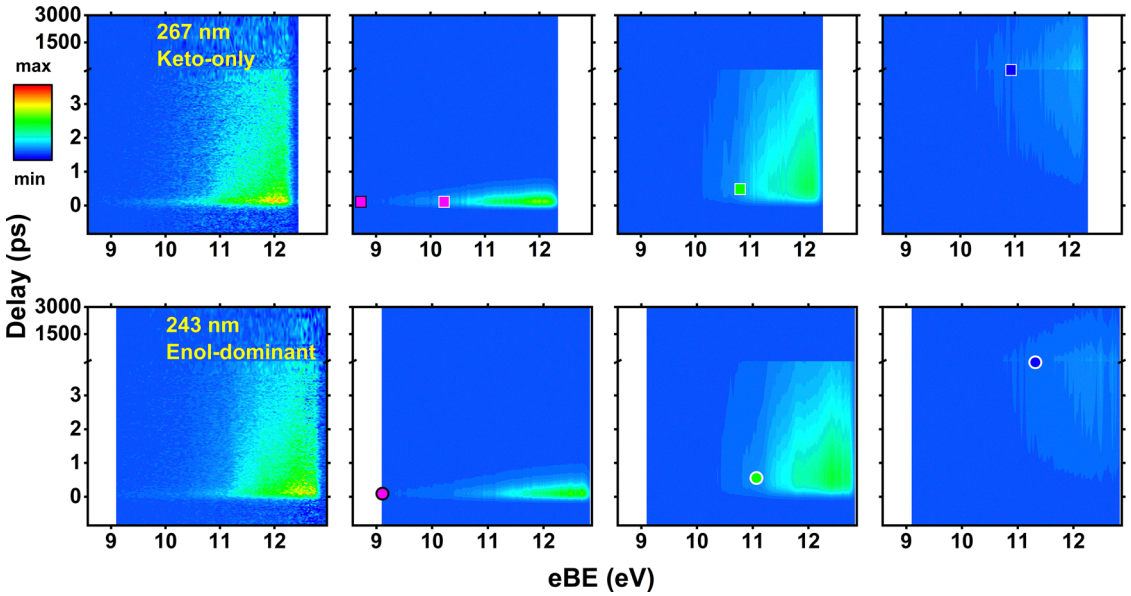

Fig. 5 TRPES components in the keto-only (267 nm, top) and enol-dominant (243 nm, bottom) spectral regions of 5-azacytosine absorption. The first column shows the TRPES signals, while the remaining columns display the individual components extracted with global analysis. The squares and dots indicate the expected electron binding energies of the photoelectron bands associated with ionization from different electronic states. Note: there is an axis break at a pump–probe delay of 4 ps.

shown that direct decay to the GS is mostly inactive and, instead, efficient IC to the lower $S_1(^1n_N\pi^*)$ state occurs on a timeframe of 40 fs.[29,30] This mechanism is supported by the sequential decay model applied in the TRPES analysis and the observation of the $S_1(^1n_N\pi^*)$ photoelectron band associated with the second decay constant in column 3 of Fig. 5. A direct deactivation from the $S_2(^1\pi\pi^*)$ back to the GS cannot be excluded on the basis of this UV pump-UV-probe TRPES experiment due to insufficient photon energy to probe ground state repopulation dynamics.

Based on the *ab initio* molecular dynamics simulation of keto 5AC,[30] the most likely decay pathway from $S_1(^1n_N\pi^*)$ is ultrafast IC to the GS, with a time constant of approximately 1 ps. The *ab initio* study also predicts ISC with a time constant of $\sim$9 ps as an alternative deactivation route with SOC of 13 cm^{-1} and a quantum yield of about 10%. This channel, although minor, is further enabled by the negligible energy barrier of $<$0.02 eV between $S_1(^1n_N\pi^*)$ to the lowest triplet state $T_1(^3\pi\pi^*)$. Hence, the second time constant of 3.6 ps, which is of the same order of magnitude as both predicted time constants, is assigned to the depopulation dynamics of the $S_1(^1n_N\pi^*)$ state along two parallel pathways branching into IC and ISC. The measured time constant represents an average of both decay processes and, due to weighted contributions from both the faster IC and the slower ISC, the measured value is in between the two corresponding predicted time constants. The observed photoelectron band appears in the higher eBE range where signals from ionization of the $S_1(^1n_N\pi^*)_{min}$ are expected (Fig. 5, column 3) and captures the population decay from the lowest singlet excited state.

The TRPES analysis at 267 nm also requires a third, low-amplitude component with a decay constant of 3.0 ns, which is attributed to ISC from the lowest triplet state back to the GS. The photoelectron band falls within the predicted energy region for ionization from the $T_1(^3\pi\pi^*)_{min}$. As expected, (see Table S2 in SI) no additional shift in the photoelectron band is observed compared to the $S_1(^1n_N\pi^*)$ ionization channel. Nevertheless, the extended nanosecond timescale and the ISC pathway characterized by theory lend strong support for this assignment.

3.5. Assignment of the photoelectron spectra of enol-dominant TRPES of 5AC

Among the employed pump wavelengths, 243 nm lies within the spectral region where the enol tautomer contributes most significantly and will dominate in the TRPES signal. However, some non-negligible contributions from the keto tautomer (Fig. 2) are to be expected (Table 3) and must be considered in the interpretation.

According to the theoretical model in section 3.2 above, the photon energy at 243 nm (5.10 eV) excites the bright $S_2(^1\pi\pi^*)$ state of enol 5AC. The $S_2(^1\pi\pi^*)$ and $S_1(^1n_N\pi^*)$ states of enol 5AC are strongly mixed and nearly degenerate and no minimum could be identified on the $S_2(^1\pi\pi^*)$ surface along the deactivation pathway. Thus, following excitation to the FC($^1\pi\pi^*$) region, enol 5AC rapidly decays directly into the $S_1(^1n_N\pi^*)_{min}$. The first photoelectron spectral component from the global TRPES analysis starts at eBEs assigned to the FC($^1\pi\pi^*$) region and significantly increases in intensity above 11 eV (Fig. 5, column 2). This photoelectron band decays with a time constant of 200 fs and is assigned to the evolution from the FC region of the $S_2(^1\pi\pi^*)$ state into the lowest singlet state, $S_1(^1n_N\pi^*)$. If instead photoexcitation is to FC($^1n_N\pi^*$), this initial step corresponds to motion on the $S_1(^1n_N\pi^*)$ hypersurface to its minimum, $S_1(^1n_N\pi^*)_{min}$. For both cases, similar shifts in the photoelectron spectrum are expected because the FC($^1\pi\pi^*$) and FC($^1n_N\pi^*$) ionization energies and Dyson norms are almost identical (Table 2). This assignment is

Table 2 Vertical and adiabatic excitation and ionization energies for the relevant geometries, computed at the XMS(6S;6T)-CASPT2(16,11)/cc-pVDZ and XMS(7S;7T)-CASPT2(14,10)/cc-pVDZ levels for keto and enol 5AC, respectively. Values provided for the FC region correspond to vertical excitation and ionization energies evaluated at the geometry of the ground state minimum. For all other geometries, the adiabatic excitation energies correspond to the energy difference between the ground state minimum and the excited state minima. The adiabatic ionization energies are obtained by adding the vertical ionization energies at the excited state minima to their adiabatic excitation energies

Tautomers	Keto 5AC			Enol 5AC		
Geometry	Excitation energy (eV)	Ionization energy (eV)	Ionization channel (Dyson norm)	Excitation energy (eV)	Ionization energy (eV)	Ionization channel (Dyson norm)
FC ($^1\pi\pi^*$)	4.92	9.01	D_0, π^{-1} (0.33)	5.28	9.21	D_0, π^{-1} (0.18)
		9.43	D_2, π^{-1} (0.12)		9.70	D_1, n^{-1} (0.10)
FC ($^1n_N\pi^*$)	—	—	—	5.27	9.22	D_0, π^{-1} (0.12)
					9.71	D_1, n^{-1} (0.18)
S_2 $(^1\pi\pi^*)_{min}$	4.47	10.04	D_1, n^{-1} (0.41)	—	—	—
S_1 $(^1n_N\pi^*)_{min}$	4.00	10.18	D_0, 41% π^{-1} & 30% n^{-1} (0.40)	4.21	10.16	D_0, n^{-1} (0.37)
T_1($^3\pi\pi^*)_{min}$	3.51	9.80	D_0, π^{-1} (0.83)	4.03	10.24	D_0, π^{-1} (0.70)

Table 3 Time constants (τ_1, τ_2, and τ_3) obtained from global lifetime analysis of the wavelength-dependent TRPES based on a three-exponential sequential decay model. The keto : enol tautomer ratios for the different excitation wavelengths are determined from the simulated tautomer spectra weighted by their linear regression coefficients Fig. 2(b). The ratios provide an estimate of the tautomer distribution in the photo-excited state that is probed in the TRPES measurements

Pump wavelength (nm)	Keto : enol ratio	Pump energy (eV)	τ_1 (fs)	τ_2 (ps)	τ_3 (ns)
267	0.84 : 0.16	4.64	160 ± 40	3.6 ± 0.1	3.0 ± 0.1
260	0.53 : 0.47	4.76	200 ± 40	5.1 ± 0.4	2.3 ± 0.1
250	0.40 : 0.60	4.96	170 ± 40	3.4 ± 0.4	2.0 ± 0.1
243	0.32 : 0.68	5.10	200 ± 40	2.6 ± 0.4	1.2 ± 0.1

substantiated by the second evolution associated photoelectron spectrum (Fig. 5, column 3) which aligns with the predicted eBE for ionization from the $S_1(n_N\pi^*)_{min}$ and decays with a time constant of 2.6 ps. Based on the calculations above, ISC is not expected in enol 5AC. The dominant depopulation mechanism in enol 5AC is IC from the $S_1(^1n_N\pi^*)$ state back to the GS but requires surmounting a substantial barrier (~0.67 eV) to access the CI. The second time constant is therefore associated with $S_1(^1n_N\pi^*)$ → GS deactivation. However, the fact that the TRPES analysis requires a long third decay component to achieve a good fit confirms that there is also a non-negligible contribution from keto 5AC to the TRPES spectrum. The third component with a time constant of 1.2 ns is assigned to the population dynamics in the triplet state of keto 5AC. In light of this, the first and second time constants extracted from the 243 nm TRPES similarly include a minor contribution (~30%, according to Table 3) from the keto tautomer. Compared to 267 nm excitation in the keto-only region, at 243 nm the keto tautomer has significantly higher internal vibrational energy and consequently undergoes faster deactivation dynamics. In terms of the enol dynamics, the extracted time constants, τ_1 and τ_2, should be considered lower estimates of the actual values.

3.6. Wavelength-dependence of tautomer contributions and their photodynamics

The intermediate pump wavelengths of 260 nm and 250 nm excite mixtures with significant contributions of both tautomers (Fig. 2 and Table 3) which complicates the interpretation of the TRPES. However, some additional insight can be gained when considering wavelength-dependent trends in tautomer ratios and time constants in the context of the picture derived from the keto-only and enol-dominant TRPES. Generally speaking, as the pump photon energy increases, the bright state is photo-excited with additional vibrational energy. The additional internal energy eases crossing of barriers along the deactivation pathway and speeds up the photodynamics. This is typically reflected in a systematic trend of decreasing time constants with increasing photon energy. Discontinuities in the trend may be attributed to photoexcitation of a higher lying bright state or a change in the deactivation mechanism, *e.g.* opening of new pathways. Applying this simplistic picture to 5AC, we would expect that decay times for each tautomer shorten with an increase in photon energy. In addition, the tautomer ratio changes with increasing contributions from the enol tautomer to the TRPES. Both effects must be considered simultaneously to interpret the extracted time constants in Table 3.

From 267 nm photoexcitation of keto 5AC, as discussed above, the time constants of 160 fs, 3.6 ps, and 3.0 ns are assigned, to $S_2(^1\pi\pi^*)$ → $S_1(^1n_N\pi^*)$ IC, subsequent depopulation of $S_1(^1n_N\pi^*)$ → GS IC with minor ISC into a long-lived triplet state, and decay of the triplet state, respectively. In a purely keto tautomeric molecular beam, these time constants are expected to decrease at shorter excitation wavelengths, and the effect should be most noticeable if there are barriers along the deactivation pathways. The first time constant, within the experimental error, remains unchanged as the pump photon energy increases. Neither excess vibrational energy nor a shift in the tautomer ratio toward enol has any significant effect on the photodynamics. This indicates highly efficient and barrierless motion from the FC($^1\pi\pi^*$) region to the $S_1(^1n_N\pi^*)$ state in both tautomers, a picture that is consistent with the theoretical models. In contrast, the second time constant shows a distinctly different wavelength-dependent behavior. At an excitation wavelength of 260 nm, the time constant increases to 5.1 ps. Because excess energy in the keto tautomer is expected to speed up the dynamics, the longer time constant is attributed to contributions from the enol tautomer. According to Table 3, keto : enol ratio at 260 nm is estimated to be 0.53 : 0.47. The enol and keto

contribution are similar, but the timescale for $S_1(^1n_N\pi^*)$ → GS IC in the enol tautomer is likely significantly longer due to the high (0.67 eV) barrier to the CI. Overall, this causes an increase in the $S_1(^1n_N\pi^*)$ decay time observed for 260 nm photoexcitation. As the excitation wavelength is decreased further, the increase in excess internal energy in both tautomers leads to the systematic trend of shortening $S_1(^1n_N\pi^*)$ lifetimes. The behavior of the third time constant differs in that it does not show the initial rise in decay time around the onset of the enol tautomer absorption at 260 nm. Given the assignment of the nanosecond decay to the triplet state lifetime, this is not surprising because ISC is predicted to be negligible in the enol tautomer. Hence, the third time constant is assigned to the triplet state of the keto tautomer only. This interpretation is visualized in Table 3, with a blue color coding of the keto-only time constants, whereas mixed contributions with a weighted average of keto and enol decay times are indicated with a combination of blue and red shading.

3.7. Photophysical models for keto and enol 5-azacytosine

The photophysical model for 5AC derived from the TRPES experiments and *ab initio* calculations is summarized in Fig. 6. After photoexcitation, both keto and enol forms of 5AC decay from the FC($^1\pi\pi^*$) region to the $S_1(^1n_N\pi^*)$ state within a time scale of approximately 200 fs. From the $S_1(^1n_N\pi^*)$ state, the decay dynamics differ between the two tautomers. For keto 5AC, dynamics simulations have shown[30] that IC from $S_1(^1n_N\pi^*)$ to the GS proceeds *via* two pathways with hopping geometries within distinct parameter spaces: (1) a boat-like conformation of the ring with N_3 and C_6 displaced from the molecular plane in the same direction, and (2) a half-chair conformation with N_5 and C_6 displaced from the ring plane in opposite directions, and an envelope-like geometry with C_6 displaced out of the ring plane. These geometries all involve ring deformation localized near the $N_5{=}C_6$ bond. The energy barrier to the boat-like pathway is only 0.07 eV, while the barrier to the half-chair pathway is 0.28 eV, making the boat-like pathway the preferred route for efficient IC to the GS. The SOC between $S_1(^1n_N\pi^*)$ and $T_1(^3\pi\pi^*)$ is only 13 cm^{-1}, but due to the minimal energy barrier of $<$0.02 eV, some ISC to the triplet state is expected. Thus, for keto 5AC, decay to the GS occurs in parallel with minor ISC to the triplet state on a timescale of 3 ps. From the triplet manifold, keto 5AC decays to the GS within ~3 ns. In contrast, for enol 5AC, no crossing point between $S_1(^1n_N\pi^*)$ and $T_1(^3\pi\pi^*)$ is identified, making ISC highly unlikely. Instead, enol 5AC undergoes direct IC from $S_1(^1n_N\pi^*)$ to the GS, which is characterized by an envelope-like geometric distortion with C_6 displaced out of the ring plane. This pathway has a relatively high energy barrier (~0.67 eV), which results in a slower IC timescale. The weighted IC timescales of keto and enol 5AC fall in the range 3–5 ps, and the actual IC time scale of enol 5AC is likely longer, consistent with its high energy barrier.

In summary, the main difference between the decay mechanisms between the two tautomers occurs after reaching their corresponding $S_1(^1n_N\pi^*)$ states. In keto 5AC, along with IC to GS, there is some ISC to triplet state, which is due to decent SOC (13 cm^{-1}) and very low energy barrier ($<$0.02 eV). In enol 5AC, however, there is no crossing point between the $S_1(^1n_N\pi^*)$ and the triplet state, and the tautomer undergoes only IC to the GS. Interestingly, the geometry of all the channels of $S_1(^1n_N\pi^*)$ → GS IC pathways in both keto and enol 5AC are characterized by displacement of C_6 out of the ring plane.

3.8. Effect of aza-substitution on the cytosine photodynamics

In the pyrimidine nucleobases, one of the primary decay pathways for a photoexcited molecule to return to the GS is IC *via CIs* characterized by elongation and twisting of the $C_5{=}C_6$

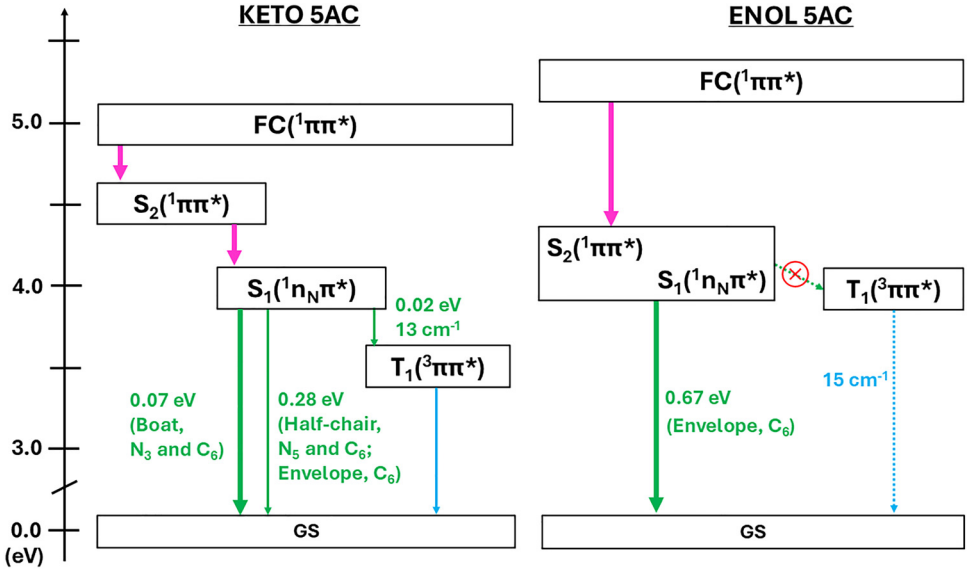

Fig. 6 Decay dynamics of keto and enol 5AC. The arrows indicate deactivation pathways from different states, with the color scheme corresponding to the different time constants: τ_1 (magenta), τ_2 (green), and τ_3 (blue). The thickness of the arrows indicates the relevance of the processes, and the dashed arrow denotes a negligible process. The numbers in eV and cm^{-1} represent the energy barriers and SOCs, respectively, at the crossing points of the states. The labels in parentheses indicate the geometries of the crossing points.

bond and out-of-plane C_6-puckering.[57,58] This raises the question of how aza-substitution of the active bond at the C_5 position alters the IC mechanism. For cytosine, the situation is complicated by the presence of keto and enol tautomers, both with multiple competing deactivation pathways, that may be affected differently by the substitution.

Based on surface-hopping dynamics simulations,[25] in keto cytosine, a 3-state near degeneracy, characterized by C_5=C_6 and C_2=O stretches, enables direct deactivation from the $S_2(^1\pi\pi^*)$ to the GS. A similar degeneracy has not been identified in 5AC and is therefore not discussed any further here. Following IC from the $S_2(^1\pi\pi^*)$ to the $S_1(^1n_O\pi^*)$ state in keto cytosine, two distinct CIs connect back to the GS. A semi-planar and a NH_2 out-of-plane CI have been identified but the relevance of the individual pathways is dependent on the level of theory as well as timescales of interest and is still up to debate.[25,28,59–62] The semi-planar CI provides a major deactivation channel from the $S_1(^1n_O\pi^*)$ state to the GS. The ring maintains near planarity, *i.e.* it undergoes mostly in-plane bond distortions including C_5=C_6 elongation, and the C_2=O is stretched. A third C_6-puckering CI is rarely frequented. Upon aza-substitution of the C_5 in the C_5=C_6 bond, geometric and electronic aspects play a role.[29] The heavier mass of the nitrogen atom and the stronger N_5=C_6 bond are expected to hamper, but not entirely inhibit, the out-of-plane displacements characteristic of the non-planar CIs or bond elongation associated with the semi-planar CI. Comparing the mechanism in keto 5AC to keto cytosine, the dominant pathways for IC from the $S_1(^1n_N\pi^*)$ to the GS remain localized near the N_5=C_6 bond. More specifically, they involve out-of-plane motion of C_6 with geometries resembling boat, half-chair and envelope-like structures. Aza-substitution further reduces branching into the already minor ISC channel. The SOC between the $S_1(^1n_N\pi^*)$ and $T_1(^3\pi\pi^*)$ in keto 5AC amounts to 13 cm^{-1} which is significantly smaller than that in keto cytosine (40 cm^{-1}). Nevertheless, the long-lived ($\sim$ns) time component observed in the TRPES demonstrates that even moderate SOC (13 cm^{-1}) combined with a very small barrier (0.02 eV) allows a fraction of the $S_1(^1n_N\pi^*)$ population to undergo ISC to the triplet state. These subtle differences in the deactivation mechanism are reflected in the observed dynamics. For example, the lifetime of the lowest singlet state, $S_1(^1n_N\pi^*)$, in keto 5AC increases compared to keto cytosine. Photoexcitation experiments of cytosine in the keto-only region, have reported time constants in the range from 0.6–1.1 ps for IC from the $S_1(^1n_O\pi^*)$ to the GS, which is more than 3 times shorter than in keto 5AC.[23,24] This finding aligns with observations in other cytosine derivatives, such as 5-methylcytosine and 5-fluorocytosine, with substitutions at the C_5 position.[27]

According to surface-hopping dynamics simulations for the enol tautomer of cytosine, NH_2 out-of-plane and C_6 puckered CIs from $S_1(^1n_N\pi^*)$ to the GS have been reported with the latter frequented more often.[25] Upon aza-substitution in the 5-position, the dominant deactivation mechanism of cytosine is preserved and $S_1(^1n_N\pi^*)$ $\rightarrow$ GS IC in enol 5AC is similarly characterized by puckering of the C_6. While the enol tautomers of both cytosine and 5AC exhibit similar IC mechanisms to the GS, comparing their photodynamics is challenging. Timescales for IC are available from dynamics simulations only for enol cytosine, but not enol 5AC. Time-resolved photoionization experiments have yielded $S_1(^1n_N\pi^*)$ depopulation times in the range of 2.3–3.8 ps (with a 260–270 nm pump) for cytosine[24] and 2.6 ps (with 243 nm pump) for 5AC. Excitation with these pump wavelengths fall within a region of the absorption spectrum where enol contributions are significant. However, these decay times are not only strongly pump wavelength dependent, but they also represent an average of multiple deactivation pathways from $S_1(^1n_N\pi^*)$ and are subject to varying keto tautomer contributions. These factors prevent a more quantitative assessment of the aza-substitution effect on the enol cytosine decay dynamics.

One major aspect that differentiates the deactivation mechanisms in cytosine and aza-cytosine lies in the orbital characteristics of the lowest singlet state. The non-bonding orbitals involved in the lowest singlet n $\rightarrow$ π^* transition in both 5AC tautomers are localized around the nitrogen atom of the pyrimidine ring, whereas in keto cytosine, the localization is around the oxygen. The enhanced ISC in keto cytosine relative to its enol form is due to localization of the orbital excitation around the carbonyl group,[25] whereas the low ISC in keto 5AC results from excitation localized around the N_5 atom instead.[30] The latter not only quenches SOCs but also facilitates efficient IC to the GS *via* a minimum energy CI. ISC is negligible in the enol tautomers of both cytosine and 5AC due to the absence of a carbonyl group. Among other aza-substituted nucleobases, the low triplet yield places keto 5AC into a distinct category, unlike 6-azauracil and 8-azaadenine which exhibit high yields following UV photoexcitation.[10]

3.9. Comparison to solution phase 5AC dynamics

The solution-phase excited-state dynamics of 5AC have been intensively investigated, with all studies performed in either acetonitrile or in PBS (aqueous phosphate buffer solution) and all assuming the presence of only the N_1–H keto form. Compared to the gas phase, the absorption band of 5AC in solution is blue shifted with a more pronounced shift in buffer solution than in acetonitrile.[10,63,64] Two independent transient absorption spectroscopy (TAS) studies of 5AC in buffer solution measured similar dynamics but differed in their interpretations. The first study revealed two time constants, 1.5 ps and 15 ps, which were attributed to a sequential decay from the photoexcited $S_2(^1\pi\pi^*)$ to $S_1(^1n_N\pi^*)$, and direct IC from $S_2(^1\pi\pi^*)$ to the GS, respectively.[63] With a broader spectral detection range and longer detection time window in the second work, similar time constants, 1.3 ps and 17 ps, were observed, but now attributed to cooling from the hot $S_1(^1n_N\pi^*)$ to its minimum, and decay from $S_1(^1n_N\pi^*)$ to the GS, respectively.[64] The IC from $S_2(^1\pi\pi^*)$ to $S_1(^1n_N\pi^*)$ is suggested to occur too rapidly to be resolvable by their TAS setup (instrument response $\sim$120 fs). Hybrid QM(CASPT2//CASSCF)/MM calculations applied to 5AC in aqueous solution predict several relaxation decay pathways from the $S_2(^1\pi\pi^*)$ state, consistent with the experimental observations.[65] The two major decay channels involve either direct IC to the ground state or IC to ground state mediated by $S_1(^1n_N\pi^*)$ *via* $S_2(^1\pi\pi^*)/S_1(^1n_N\pi^*)$ CI. The theoretical work also identifies minor decay channels involving

ISC processes, which are inefficient and slow due to small SOC at the singlet–triplet crossing points. In nanosecond laser flash photolysis of 5AC in acetonitrile, the triplet population is also experimentally found to be negligible.[10] Using QM/MM (OM2/MNDO) simulations with explicit water molecules as the solvent environment, the lifetimes of the $S_2(^1\pi\pi^*)$ and $S_1(^1n_N\pi^*)$ are estimated to be 30 fs and 12 ps, respectively.[66] In contrast, the same method applied to isolated keto 5AC yields lifetimes of 45 fs for $S_2(^1\pi\pi^*)$ and 194 ps for $S_1(^1n_N\pi^*)$.[67] Several conclusions can be drawn from these studies. Firstly, the simulations accurately reproduce the $S_1(^1n_N\pi^*)$ lifetime in solution, however a direct comparison of the theoretical and experimental $S_2(^1\pi\pi^*)$ decay time constant is not possible due to the limited time-resolution of the TAS experiments. Secondly, the simulations suggest that solvent effects significantly influence the decay dynamics of 5AC, particularly those associated with the $S_1(^1n_N\pi^*)$. Thirdly, the simulations of the 5AC dynamics predict much slower $S_1(^1n_N\pi^*)$ dynamics in the gas phase. This latter prediction is incompatible with observations from the keto-only (267 nm) TRPES in the present study with lifetimes of 160 fs, 3.6 ps, and 3 ns for the $S_2(^1\pi\pi^*)$, $S_1(^1n_N\pi^*)$ and $T_1(^3\pi\pi^*)$ states, respectively, which are more in line with SHARC simulations.[30] From a purely experimental point of view, the 5AC photodynamics in the gas phase are slightly faster than in solution, except for a minor, but long-lived triplet state channel that is present only in the gas phase.

4. Conclusion

A combination of XMS-CASPT2/cc-pVDZ calculations and TRPES experiments is employed to investigate the excited-state dynamics of the keto and enol forms of 5AC. Following photoexcitation, both tautomers rapidly decay from the FC($^1\pi\pi^*$) region to the lowest excited singlet state, $S_1(^1n_N\pi^*)$, within approximately 200 fs from where they efficiently undergo IC to the ground state within 3–5 ps. However, in keto 5AC, the moderate SOC of 13 cm^{-1} and the negligible energy barrier of <0.02 eV between the $S_1(^1n_N\pi^*)$ and triplet state account for very small, but measurable ISC and subsequent decay to the GS on much longer timescales of $\sim$3 ns. In contrast, enol 5AC has no crossing point between the $S_1(^1n_N\pi^*)$ and triplet state, favoring direct IC to the GS. When comparing keto and enol cytosine with their 5AC counterparts, aza-substitution introduces some significant differences. For example, in keto 5AC, the $N_5{=}C_6$ bond becomes shorter compared to $C_5{=}C_6$ of keto cytosine, and the non-bonding orbital of the S_1 state is localized around the endocyclic nitrogen *i.e.*, $S_1(^1n_N\pi^*)$, rather than the oxygen of the carbonyl group *i.e.*, $S_1(^1n_O\pi^*)$, as in cytosine. Given the significance of the carbonyl group in promoting ISC, these changes in the orbital localization directly impact the electronic relaxation mechanism. Nevertheless, the present study has shown that measurable ISC occurs in keto 5AC, but not in its enol tautomer.

Conflicts of interest

There are no conflicts to declare.

Data availability

The manuscript and supplementary information (SI) provide all technical details regarding the experiment and *ab initio* calculations. The raw experimental data sets, which are saved in a custom format, and the input/output files for the calculations are available upon request.

The supplementary information contains all data supporting the article. Tables: orbital transitions of enol 5AC; excited-state energies, vibrational energies, ionization energies, and electron binding energies at different geometries of keto and enol 5AC; expected shifts in TRPES plots along the electron binding energy axis at different pump wavelengths; IR spectra calculations of keto and enol 5AC; and cartesian coordinates of optimized geometries. Figures: active spaces and orbital transitions; simulated UV-vis absorption spectra of keto and enol 5AC with contributions from different states; composite linear regression fit residuals; FTIR spectra of 5AC; TRPES analysis of 5AC; justification of fits; and optimized geometries. Equations: Three-step sequential exponential decay function, and spin-orbit coupling (SOC). See DOI: https://doi.org/10.1039/d6cp00065a.

Acknowledgements

This work is supported by National Science Foundation grants CHE-1800050, CHE-2106353, CHE-2135351, and CHE-2154852. BD and SU would like to thank Moti Raj Chudali and Md Mehade Hasan for assistance in the laboratory. ACB thanks CNPq (Conselho Nacional de Desenvolvimento Científico e Tecnológico) for research fellowship (Project numbers 311821/2021-9 and 306596/2024-5). The authors thank STI (Superintendência de Tecnologia da Informação) of the University of São Paulo and the support by CENAPAD-SP (National Center for High Performance Computing - São Paulo) under the UNICAMP/FINEP - MCTI project. We also thank the Coaraci Supercomputer for computer time (FAPESP grant 2019/17874-0) and the Center for Computing in Engineering and Sciences at UNICAMP (FAPESP grant 2013/08293-7).

References

1 R. Improta, F. Santoro and L. Blancafort, *Chem. Rev.*, 2016, **116**, 3540–3593.
2 K. Kleinermanns, D. Nachtigallová and M. S. de Vries, *Int. Rev. Phys. Chem.*, 2013, **32**, 308–342.
3 C. Canuel, M. Mons, F. Piuzzi, B. Tardivel, I. Dimicoli and M. Elhanine, *J. Chem. Phys.*, 2005, **122**, 074316.
4 S. Ullrich, T. Schultz, M. Z. Zgierski and A. Stolow, *Phys. Chem. Chem. Phys.*, 2004, **6**, 2796–2801.
5 H. Kang, K. T. Lee, B. Jung, Y. J. Ko and S. K. Kim, *J. Am. Chem. Soc.*, 2002, **124**, 12958–12959.
6 A. C. Rios and Y. Tor, *Isr. J. Chem.*, 2013, **53**, 469–483.
7 A. A. Beckstead, Y. Zhang, M. S. de Vries and B. Kohler, *Phys. Chem. Chem. Phys.*, 2016, **18**, 24228–24238.
8 S. Ullrich, Y. Qu, A. Mohamadzade and S. Shrestha, *J. Phys. Chem. A*, 2022, **126**, 8211–8217.

9 B. Duwal, I. Eder, L. González, S. Mai and S. Ullrich, *Chem. Sci.*, 2025, **16**, 15015–15028.
10 T. Kobayashi, H. Kuramochi, Y. Harada, T. Suzuki and T. Ichimura, *J. Phys. Chem. A*, 2009, **113**, 12088–12093.
11 T. Kobayashi, Y. Harada, T. Suzuki and T. Ichimura, *J. Phys. Chem. A*, 2008, **112**, 13308–13315.
12 J. P. Gobbo, A. C. Borin and L. Serrano-Andrés, *J. Phys. Chem. B*, 2011, **115**, 6243–6251.
13 M. R. Chudali and S. Ullrich, *J. Phys. Chem. A*, 2025, **129**, 9279–9290.
14 M. Richter, S. Mai, P. Marquetand and L. González, *Phys. Chem. Chem. Phys.*, 2014, **16**, 24423–24436.
15 D. Faccialà, M. Bonanomi, B. N. C. Tenorio, L. Avaldi, P. Bolognesi, C. Callegari, M. Coreno, S. Coriani, P. Decleva, M. Devetta, N. Došlić, A. De Fanis, M. Di Fraia, F. Lever, T. Mazza, M. Meyer, T. Mullins, Y. Ovcharenko, N. Pal, M. N. Piancastelli, R. Richter, D. E. Rivas, M. Sapunar, B. Senfftleben, S. Usenko, C. Vozzi, M. Gühr, K. C. Prince and O. Plekan, *J. Am. Chem. Soc.*, 2025, **147**, 30694–30707.
16 S. Karashima and T. Suzuki, *J. Phys. Chem. Lett.*, 2025, **16**, 12045–12049.
17 L. Fu, Z. Wang, Y. Liu, X. Wang, R. Xu, W. Liu, J. Chen and J. Xu, *J. Photochem. Photobiol., A*, 2020, **396**, 112491.
18 J. P. Gobbo and A. C. Borin, *J. Phys. Chem. B*, 2012, **116**, 14000–14007.
19 A. V. Sanches de Araújo and A. C. Borin, *J. Phys. Chem. A*, 2019, **123**, 3109–3120.
20 E. Nir, M. Müller, L. I. Grace and M. S. de Vries, *Chem. Phys. Lett.*, 2002, **355**, 59–64.
21 G. Bazsó, G. Tarczay, G. Fogarasi and P. G. Szalay, *Phys. Chem. Chem. Phys.*, 2011, **13**, 6799–6807.
22 Y. Podolyan, Y. V. Rubin and J. Leszczynski, *J. Phys. Chem. A*, 2000, **104**, 9964–9970.
23 J.-W. Ho, H.-C. Yen, W.-K. Chou, C.-N. Weng, L.-H. Cheng, H.-Q. Shi, S.-H. Lai and P.-Y. Cheng, *J. Phys. Chem. A*, 2011, **115**, 8406–8418.
24 K. Kosma, C. Schröter, E. Samoylova, I. V. Hertel and T. Schultz, *J. Am. Chem. Soc.*, 2009, **131**, 16939–16943.
25 S. Mai, P. Marquetand, M. Richter, J. González-Vázquez and L. González, *Chem. Phys. Chem.*, 2013, **14**, 2920–2931.
26 M. Ruckenbauer, S. Mai, P. Marquetand and L. González, *Sci. Rep.*, 2016, **6**, 35522.
27 R. J. Malone, A. M. Miller and B. Kohler, *Photochem. Photobiol.*, 2003, **77**, 158–164.
28 A. Nakayama, Y. Harabuchi, S. Yamazaki and T. Taketsugu, *Phys. Chem. Chem. Phys.*, 2013, **15**, 12322–12339.
29 A. Giussani, M. Merchán, J. P. Gobbo and A. C. Borin, *J. Chem. Theory Comput.*, 2014, **10**, 3915–3924.
30 A. Carlos Borin, S. Mai, P. Marquetand and L. González, *Phys. Chem. Chem. Phys.*, 2017, **19**, 5888–5894.
31 H. Yu, N. L. Evans, V. G. Stavros and S. Ullrich, *Phys. Chem. Chem. Phys.*, 2012, **14**, 6266–6272.
32 N. L. Evans, H. Yu, G. M. Roberts, V. G. Stavros and S. Ullrich, *Phys. Chem. Chem. Phys.*, 2012, **14**, 10401–10409.
33 N. L. Evans and S. Ullrich, *J. Phys. Chem. A*, 2010, **114**, 11225–11230.
34 D. M. P. Holland, M. A. MacDonald, M. A. Hayes, P. Baltzer, B. Wannberg, M. Lundqvist, L. Karlsson and W. V. Niessen, *J. Phys. B: At., Mol. Opt. Phys.*, 1996, **29**, 3091–3107.
35 J. J. Snellenburg, S. Laptenok, R. Seger, K. M. Mullen and I. H. M. van Stokkum, *J. Stat. Softw.*, 2012, **1**(3), 2012.
36 *OriginPro*, OriginLab Corporation, Northampton, MA, USA, 2022 edn.
37 A. A. Granovsky, *J. Chem. Phys.*, 2011, **134**, 214113.
38 T. Shiozaki, W. Győrffy, P. Celani and H.-J. Werner, *J. Chem. Phys.*, 2011, **135**, 081106.
39 T. H. Dunning Jr, *J. Chem. Phys.*, 1989, **90**, 1007–1023.
40 K. Andersson, P. Å. Malmqvist and B. O. Roos, *J. Chem. Phys.*, 1992, **96**, 1218–1226.
41 G. Ghigo, B. O. Roos and P.-Å. Malmqvist, *Chem. Phys. Lett.*, 2004, **396**, 142–149.
42 J. P. Zobel, J. J. Nogueira and L. González, *Chem. Sci.*, 2017, **8**, 1482–1499.
43 G. Li Manni, I. F. Galván, A. Alavi, F. Aleotti, F. Aquilante, J. Autschbach, D. Avagliano, A. Baiardi, J. J. Bao, S. Battaglia, L. Birnoschi, A. Blanco-González, S. I. Bokarev, R. Broer, R. Cacciari, P. B. Calio, R. K. Carlson, R. Carvalho Couto, L. Cerdán, L. F. Chibotaru, N. F. Chilton, J. R. Church, I. Conti, S. Coriani, J. Cuéllar-Zuquin, R. E. Daoud, N. Dattani, P. Decleva, C. de Graaf, M. G. Delcey, L. De Vico, W. Dobrautz, S. S. Dong, R. Feng, N. Ferré, M. Filatov, L. Gagliardi, M. Garavelli, L. González, Y. Guan, M. Guo, M. R. Hennefarth, M. R. Hermes, C. E. Hoyer, M. Huix-Rotllant, V. K. Jaiswal, A. Kaiser, D. S. Kaliakin, M. Khamesian, D. S. King, V. Kochetov, M. Krośnicki, A. A. Kumaar, E. D. Larsson, S. Lehtola, M.-B. Lepetit, H. Lischka, P. López Ríos, M. Lundberg, D. Ma, S. Mai, P. Marquetand, I. C. D. Merritt, F. Montorsi, M. Mörchen, A. Nenov, V. H. A. Nguyen, Y. Nishimoto, M. S. Oakley, M. Olivucci, M. Oppel, D. Padula, R. Pandharkar, Q. M. Phung, F. Plasser, G. Raggi, E. Rebolini, M. Reiher, I. Rivalta, D. Roca-Sanjuán, T. Romig, A. A. Safari, A. Sánchez-Mansilla, A. M. Sand, I. Schapiro, T. R. Scott, J. Segarra-Martí, F. Segatta, D.-C. Sergentu, P. Sharma, R. Shepard, Y. Shu, J. K. Staab, T. P. Straatsma, L. K. Sørensen, B. N. C. Tenorio, D. G. Truhlar, L. Ungur, M. Vacher, V. Veryazov, T. A. Voß, O. Weser, D. Wu, X. Yang, D. Yarkony, C. Zhou, J. P. Zobel and R. Lindh, *J. Chem. Theory Comput.*, 2023, **19**, 6933–6991.
44 F. Aquilante, T. B. Pedersen and R. Lindh, *J. Chem. Phys.*, 2007, **126**, 194106.
45 F. Aquilante, P.-Å. Malmqvist, T. B. Pedersen, A. Ghosh and B. O. Roos, *J. Chem. Theory Comput.*, 2008, **4**, 694–702.
46 T. B. Pedersen, S. Lehtola, I. F. Galván and R. Lindh, *Wiley Interdiscip. Rev.: Comput. Mol. Sci.*, 2024, **14**, e1692.
47 B. O. Roos, in *Advances in Chemical Physics*, 1987, pp. 399–445.
48 P.-Å. Malmqvist and B. O. Roos, *Chem. Phys. Lett.*, 1989, **155**, 189–194.
49 Y. Nishimoto, S. Battaglia and R. Lindh, *J. Chem. Theory Comput.*, 2022, **18**, 4269–4281.
50 B. A. Heß, C. M. Marian, U. Wahlgren and O. Gropen, *Chem. Phys. Lett.*, 1996, **251**, 365–371.
51 P. Å. Malmqvist, B. O. Roos and B. Schimmelpfennig, *Chem. Phys. Lett.*, 2002, **357**, 230–240.

52 B. O. Roos and P.-Å. Malmqvist, *Phys. Chem. Chem. Phys.*, 2004, **6**, 2919–2927.
53 X. Zhu, K. C. Thompson and T. J. Martínez, *J. Chem. Phys.*, 2019, **150**, 164103.
54 B. N. Tenorio, A. Ponzi, S. Coriani and P. Decleva, *Molecules*, 2022, **27**(4), 1203.
55 J. P. Dahl and M. Springborg, *J. Chem. Phys.*, 1988, **88**, 4535–4547.
56 R. Schinke, *Photodissociation Dynamics: Spectroscopy and Fragmentation of Small Polyatomic Molecules*, Cambridge University Press, Cambridge, 1993.
57 M. Merchán, R. González-Luque, T. Climent, L. Serrano-Andrés, E. Rodríguez, M. Reguero and D. Peláez, *J. Phys. Chem. B*, 2006, **110**, 26471–26476.
58 J. Cuéllar-Zuquin, A. J. Pepino, I. F. Galván, I. Rivalta, F. Aquilante, M. Garavelli, R. Lindh and J. Segarra-Martí, *J. Chem. Theory Comput.*, 2023, **19**, 8258–8272.
59 K. A. Kistler and S. Matsika, *J. Phys. Chem. A*, 2007, **111**, 2650–2661.
60 M. Barbatti, A. J. A. Aquino, J. J. Szymczak, D. Nachtigallová and H. Lischka, *Phys. Chem. Chem. Phys.*, 2011, **13**, 6145–6155.
61 H. R. Hudock and T. J. Martínez, *Chem. Phys. Chem.*, 2008, **9**, 2486–2490.
62 L. Blancafort, *Photochem. Photobiol.*, 2007, **83**, 603–610.
63 Z. Zhou, X. Zhou, X. Wang, B. Jiang, Y. Li, J. Chen and J. Xu, *J. Phys. Chem. A*, 2017, **121**, 2780–2789.
64 Z. Chen, X. Wang, M. Jia, X. He, H. Pan and J. Chen, *Photochem. Photobiol.*, 2024, **100**, 291–297.
65 X.-P. Chang, L. Zheng, L. Yu, T.-S. Zhang and B.-B. Xie, *Phys. Chem. Chem. Phys.*, 2022, **24**, 27793–27803.
66 O. Tichý, M. Pederzoli, J. Pittner and J. V. Burda, *J. Chem. Theory Comput.*, 2023, **19**, 1976–1985.
67 O. Tichý and J. V. Burda, *J. Mol. Struct.*, 2022, **1250**, 131863.

